Contrast enhancement of surface layers with fast middle-infrared scanning

Tim Kümmel [a,c,*], Tobias Teumer [a,b], Patrick Dörnhofer [a], Frank-Jürgen Methner [b], Björn Wängler [c], Matthias Rädle [a]

[a] Center for Mass Spectrometry and Optical Spectroscopy, Mannheim University of Applied Sciences, Paul-Wittsack-Str. 10, Mannheim, 68163, Germany
[b] Institute of Food Technology and Food Chemistry, Technische Universität Berlin, Seestraße 13, Berlin, 13353, Germany
[c] University of Heidelberg, Medical Faculty Mannheim, Theodor-Kutzer-Ufer 1-3, Mannheim, 68167, Germany

ARTICLE INFO

ABSTRACT

In this study, we present an efficient and innovative method to visualize absorption differences in the mid-infrared range with spatial resolution using laser technology. We focus on only two lasers with wavelengths between 3.4 μm and 3.6 μm and a spatial resolution of 20 μm and thus achieve a scanning speed up to 300 kS/s for fast image generation. In this article, we focus especially on the detection of C–H bands in this region of the absorption spectrum. Concealed structures are examined by calculating the measured structures with both wavelengths. In our results, we demonstrate exemplary measurements on 130-μm-thick polyvinyl chloride layers. In turn, these structures are suitable for further processing in rapid quantitative quality control.

1. Introduction

The possibility of differentiating between two or more substances is gaining significant importance in quality control [1]. In particular, contactless optical control procedures are used, which provide surface adequate information about the current relevant-conditions [2, 3, 4], including monitoring with X-ray photoelectron spectroscopy [5] and ultrasound [6]. Due to the increasing complexity of sample measurement, the measuring equipment must also improve to meet the respective requirements [7]. Photoacoustic [8], terahertz techniques [9, 10] and Fourier transform infrared (FT-IR) mapping [11] are budding measurement systems for complex analysis and discrimination of materials. The development of materials can also be better coordinated with the aid of this measuring method [12]. FT-IR measurement has been used widely in medical technologies [13], but it is increasingly used in quality control applications [14]. A major advantage of this measurement method is the spectral high resolution mid-infrared information content of measured targets. Additional information about the molecular structure of a sample based on absorption differences in the middle-infrared (MIR) is provided. However, one acquired FT-IR spectrum includes more information than is actually required for desired applications. High measurement periods

and subsequent complex sorting with clustering of recorded data reflect this [15]. In this study, we present a measurement method that aims at rapid scanning of absorption differences in the mid-infrared wavelength range, especially between 3.4 μm and 3.6 μm.

There are also selected imaging methods in the mid-infrared range in this field of application, which use so-called camera-based systems [16, 17, 18]. In this sense, the camera represents a focal plane array (FPA) [16] or video graphics arrays (VGA) for particularly high frame rates [17]. The measurement time can range between 11 s and 0.02 s, for an image field of 2.5 cm^2, depending on the method. Nevertheless, the two systems mentioned have significant disadvantages. They both require complex illumination of the entire image field. In addition, the samples have to be very thin because they are imaged by transmissive measurement. The advantage of the technique presented by us is the measurement on samples of various thicknesses, because we measure the direct reflex. In addition, the image field does not have to be permanently fully illuminated, since we work with a flying spot. Only the current measuring point is illuminated. Thus, larger and variable scan fields (25 cm^2) can be realized by a constant resolution. FT-IR-Imaging methods that also work with FPA chips [15] come closest to the technology presented. However, we only record two wavelengths and not an entire spectrum. Thereby,
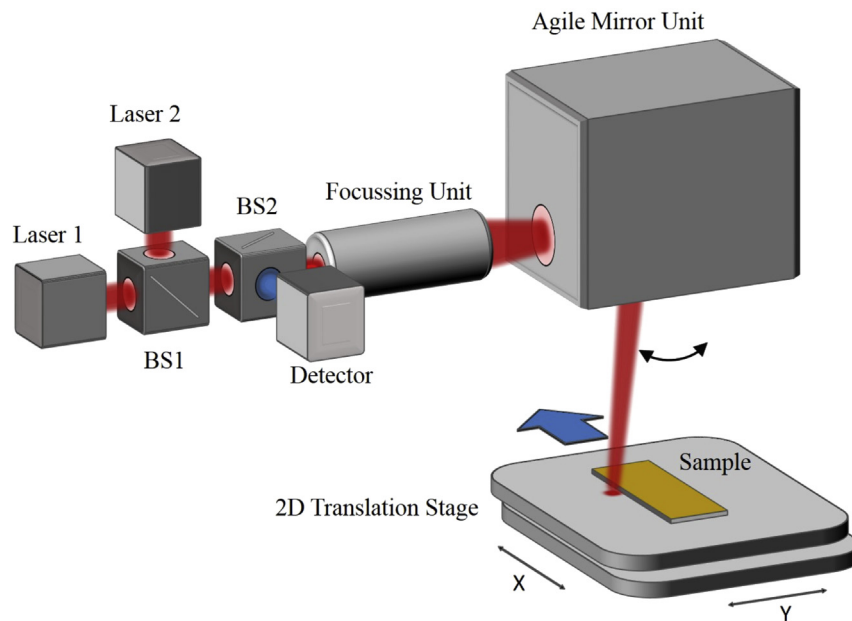

Fig. 1. Schematic view of the MIR scanner setup. The laser beam is focused on the specimen by the focusing lens unit. The agile mirror unit enables the use of the deflecting beam light. The linear unit moves orthogonally to the deflection direction of the laser beam. The detector is confocally mounted in the optical pathway of the laser light. Beam splitters (BS) are integrated in the optical path to guide the excitation light and the measurement signal.
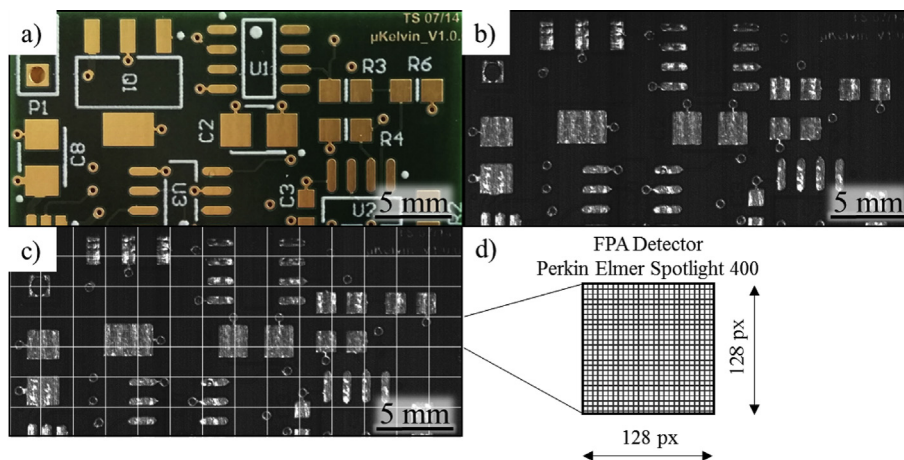

Fig. 2. Comparison of MIR scanner to FT-IR Imaging (Perkin Elmer Spotlight 400) using a test target (circuit board). a) Visual image. b) Scan result with MIR scanner for the wavelength 3417 nm; scan field: 1500 × 750 px; spatial resolution: 20 μm; scan duration: 10 s c) Scan pattern for stitching with the FT-IR imager from Perkin Elmer (Spotlight 400) to get comparable results the MIR scanner. d) FPA detector size from Perkin Elmer Spotlight 400.

our technology clearly stands out when considering the scanning speed and larger scanning areas (>1 cm^2) which do not have to be stitched together as with the automatically guided FT-IR [15].

In contrast to camera-based mid-infrared imaging systems [18], we demonstrate that spatially resolved discrimination of absorption properties is possible by spot-scanning sample surfaces of 50 cm^2. In this context, we show the possibility to ray thin polymer layers in the mentioned mid-infrared range and visualize underlying hidden structures with high sampling rates.

2. Materials and methods

The MIR scanner presented essentially consists of two different lasers, a focusing unit, an agile mirror system and a two-dimensional linear translation stage (Fig. 1). In this scanning process, the laser beam is deflected across the sample, similar to a common flying-spot scanner [19]. By means of the translation stage, the sample is moved orthogonally

to the direction of the laser beam deflection. The interaction between laser beam deflection and translation stage movement generates a two-dimensional measurement field, resulting in a measurement image. Image distortion is reduced by interaction of the components. Detection and thus data acquisition of the measurement signal is confocal. Beam splitters (BS) link optical components (lasers and detector) for the confocal beam path. Thus, the illuminating laser light (Laser 1 and Laser 2) and confocal detection signal pass through the focusing unit of the same optical pathway. During the measuring process, the laser light is focused on the sample. The setup described enables a measuring area of 50 cm^2 scannable with a spatial resolution of 20 μm. A distance of 12 cm separates the optical system from the target on the translation stage.

Synchronization between the mechanical and optical components is achieved by signal processing at the detector and the mirror unit, as well as by mathematical correlations between the deflection of the laser beam and the displacement of the translation stage. During the scan operation, image pixels are generated at a sample rate of up to 300 kS/s.
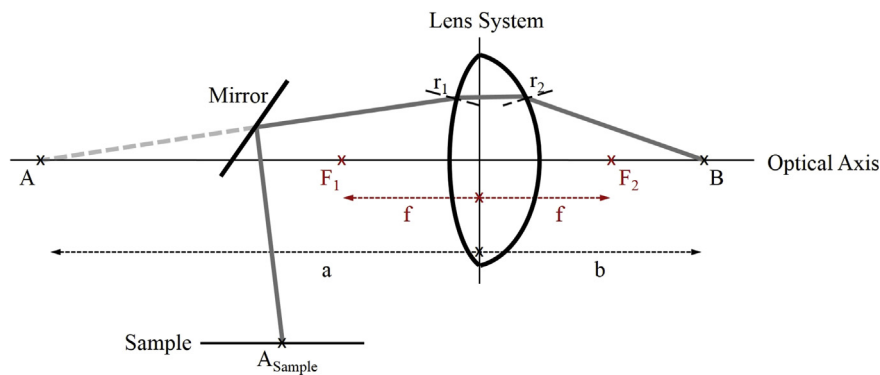
Fig. 3. Schematic representation of the lens theory for the MIR scanner. The lens system is to be considered as an analogue to a real lens system. For object width *a*, *A* = *A_Sample* is applied. *A* represents the object spot to be imaged on *B* (image point). The focal length *f* indicates the focal point on the object side with F_1 and on the image side with F_2.

The presented MIR scanner is compared to camera- or FPA-based systems in Fig. 2. Fig. 2a shows a visual image of a circuit board. Fig. 2b shows the same section, but it is scanned with the MIR scanner at the wavelength 3417 nm. The scanning speed was 300 kS/s and the spatial resolution 20 μm. The image segment consists of 1500 × 750 px, which corresponds to an area of 4.5 cm^2, and was acquired in approx. 10 sec including calculation time.

The same area is visualized using, the FPA-based scanning system Perkin Elmer Spotlight 400, which acquires multiple images adjacent to each other and combines the generated data to form an entire image. The pattern shown in Fig. 2c depicts the scanning pattern of the Spotlight 400. The FPA detector of the Spotlight 400 (Fig. 2d) consists of 128 × 128 px [20] and can achieve a spatial resolution of 20 μm with appropriately adapted optics. For rougher resolutions, the scan grid (Fig. 2c) is larger meshed and for smaller resolutions finer meshed. Due to the stitching of the images and the acquisition of several spectra in combination with sufficient exposure time, a comparable scan with the Spotlight 400 would require about 2 h. Finer resolutions would be possible but would increase the scanning time significantly [15].

3. Theory/calculation

3.1. Optical characteristics

The optical scanner setup is based on essential properties of lenses such as focusing, scattering and parallelizing [21]. These properties, also valid in the mentioned mid-infrared range, are used to focus the monochromatic laser light [22]. A spot size of 50 μm is achieved on the target. Excluding the mirror system, the working distance between the lens system and the sample is 30 cm. In a simplified form, the optimized lens system is subject to the optical relationships in Eq. (1) [23].

$$\frac{1}{a} + \frac{1}{b} = (n-1) * \left(\frac{1}{r_1} - \frac{1}{r_2} \right) = \frac{1}{f} \tag{1}$$

The optical design primarily accounts for the object distance *a* and the image distance *b*. This results in a correlation between material-dependent refractive index *n* and radii of curvature of the entrance and exit lenses r_1 and r_2. Fig. 3 schematically shows the correlation between the parameters described. This lens should be considered as a
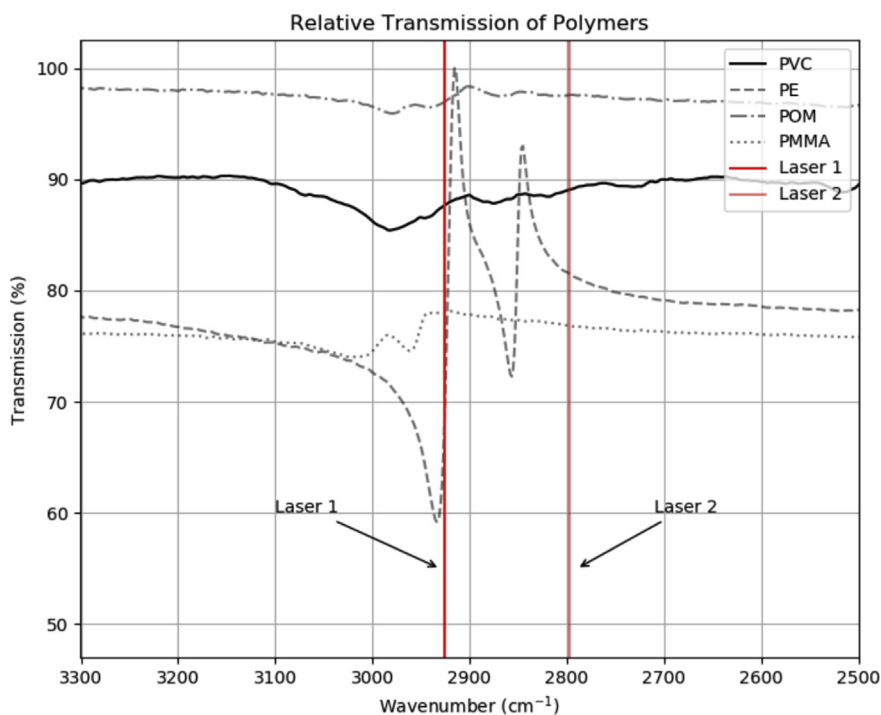

Fig. 4. Relative transmission of preselected polymers. Polyvinyl chloride (PVC) exhibits linear behaviour. The wavenumbers of the lasers are placed in the band between 2980 cm^{-1} and 2700 cm^{-1}. The wavenumber 2926 cm^{-1} is provided by Laser 1, and wavenumber 2797 cm^{-1} is provided by Laser 2.
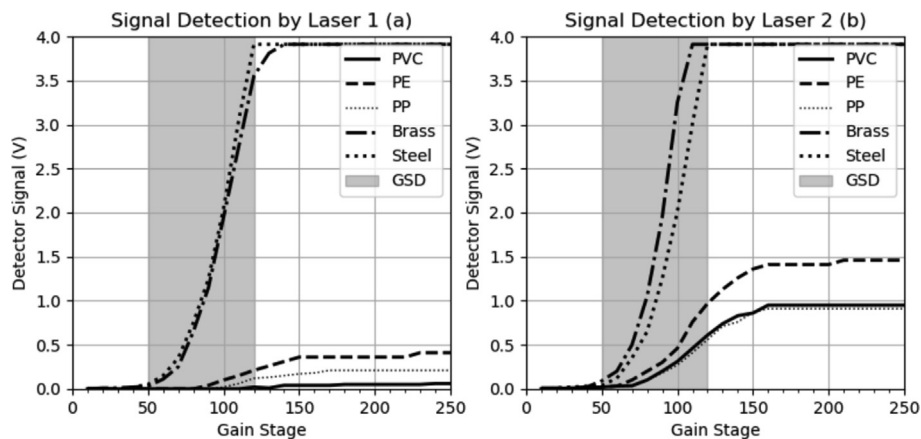
Fig. 5. Comparison of the signal intensity at the detector for polymers and metal by using Laser 1 and Laser 2. (a) Polymers are weakly detectable. (b) Polymers have a distinct signal intensity. A good signal difference (GSD) is in the gain range between 50 and 120. The difference is best at a level of 120.

representative replacement system [18] for the focusing unit. By varying the mathematical ratios, theoretical limits of the system are determined, as shown in Eq. (1), which also define the framework conditions of the focusing unit. The focus point can be adjusted by movable lenses in the optical path.

The assumption $A = A_{Sample}$ is valid for each object point with guided focusing as indicated in Fig. 3. A represents the theoretical object point on the optical axis. By placing a mirror inside the system, the object point A is deviated in the desired spatial direction. The resulting deviated object point is marked as A_{Sample}. The image point B does not vary in this context. The focal length f of the optical system also remains constant. For confocal image acquisition, the object point B of the laser light source and the detector need to be equal. All optical components of this setup are designed especially for the selected mid-infrared range.

3.2. Material properties

The application of the Lambert-Beer law in MIR spectroscopy applies to the MIR scanner presented here. Material-dependent absorption properties of the introduced laser wavelengths are determined during the passage of laser light through the sample. The determination of the associated decrease in intensity depends on the wavelength. The resulting transmission measurement of DRIFTS (diffuse reflectance infrared Fourier transform spectroscopy) performed here is based on a gold standard for each measurement. The results are used to prepare for measurement with the MIR scanner.

The special transmission here (Eq. (2)) is composed of the ratio of the gold-related reference measurement I_0 to the measurement of the sample I [24]. The transmission T is calculated from the measured absorption A. During this process, the light beam passes twice through the sample as it penetrates the sample and exits the sample through direct scattering. Therefore, the transmission is squared in calculating the absorption.

$$T^2 = (I/I_0)^2 = e^{-A} \tag{2}$$

Consequently, the measured absorption A is a negative decadal logarithm of transmission T (Eq. (3)). The transmission T is comparable to Eq. (2), but the measured parameter I_0 can also refer to a background material (e.g. metal). The value I represents the measured intensity of the target substance. In this case, the absorption is proportional to the specific sample concentration c, the thickness of the sample material d and the material-dependent extinction coefficient ε [25]. The double passage of the light beam through the sample halves the coefficients (Eq. (3)).

$$A = -log(T^2) \rightarrow -log\left(\frac{I}{I_0}\right) = \frac{c*d*\varepsilon}{2} \tag{3}$$

This specification of the transmission not only improves the comparability with literature values but also enables conclusions about the transparency of the material. For this reason, preliminary tests were performed with polymers using the DRIFT method. In Fig. 4, the results are presented in a standardized format. All examined polymers exhibit peaks at 2960 cm^{-1}, 2900 cm^{-1} and at 2880 cm^{-1} as commonly observed within the examined measuring ranges between 3300 cm^{-1} and 2500 cm^{-1}. PMMA presents an approximately inverse course. In this wavelength range, the C–H-dependent molecular vibrations exhibit significant peaks and troughs. With regard to the measurement system, the aim is to set one laser (Laser 1) at a transmission minimum and to adjust the second laser (Laser 2) at a transmission maximum. This results in the largest possible absorption difference between the two lasers and correspondingly the differences of substrate material I_0 (Laser 2) and target substance I (Laser 1). The two laser wavelengths are selected to be in the same vibrational band in which C–H bonds absorb. Thus, fluctuations in material concentration or superimpositions with other vibration bands are approximately eliminated. Therefore, laser 1 is set to the wavelength $\lambda = 3417$ nm (2926 cm^{-1}) and laser 2 to $\lambda = 3584$ nm (2797 cm^{-1}). Hence, the wavenumbers of the lasers are in the decreasing band of PVC between 2980 cm^{-1} and 2700 cm^{-1}. The lasers are distributed feedback (DFB) lasers operating in CW mode and providing 11 mW of power.

3.3. Material characteristics by MIR scanning

This system is not based on the detection of transmitted light but on the detection of reflected laser light. After passing through a surface layer twice, the laser light collides with the detector confocally. However, since the absorption or transmission of the sample is related to the reflection, the transmission can be measured with the MIR scanner indirectly, similar to DRIFTS. A transmission reflection measurement can be described for each measuring point on the sample and is based on determining the intensity at the measured point. Accordingly, low intensities indicate high absorption. However, the measured intensity depends on the sensitivity of the detector and the associated amplifier stage. The experimental results of single-point measurement on polymers and metals are presented in Fig. 5. The measurement results demonstrate that pre-amplification has a significant influence on the measurement signal. When the detector is saturated (4 V), overexposure occurs, which can be confused with low absorption. Thus, with low detection signal, compared to saturation of the detector, a high absorption of the investigated substance is to be assumed. In addition, the measurement results reveal the possibility of saturation in polymers as well. This occurs when the reflection of the sample surface outweighs the absorption of the polymer. Metals cannot be assumed to behave in this manner because they have no
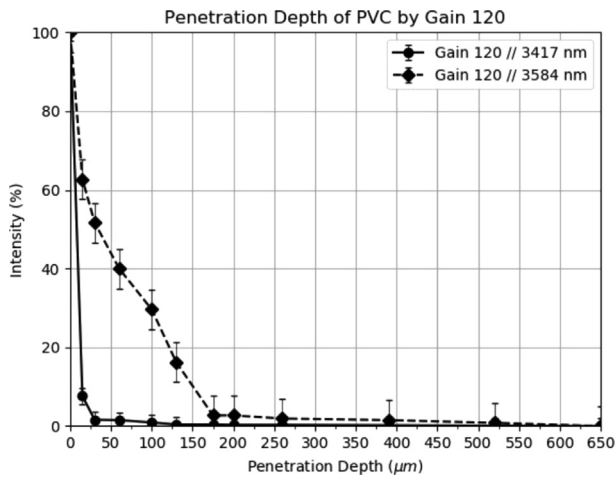
Fig. 6. Determination of the penetration depth using the pre-amplification stage 120. The maximum penetration depth for the wavelength 3417 nm is 20 μm, and for the wavelength 3584 nm, it is 150 μm.

absorption in this wavelength range. Therefore, the detection signal of metals can be traced back to the direct confocal reflection of the laser beam on the detector.

In further preliminary tests, the largest difference in signal intensity between metal and polymers was found in the range between pre-amplification 50–120. This is especially valid for the gain of 120, since metal leads to an approximate saturation of the detector and the gloss of
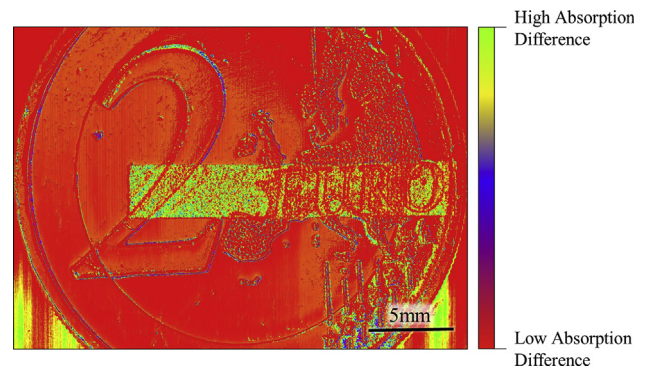

Fig. 8. Representation in pseudo colours of the absorption differences by determining the absorbance between the measurement results of the wavelengths 3417 nm and 3584 nm. All red coloured parts of the image are identical for both wavelengths. All yellow and green coloured image components show absorption differences.

the polymers is not saturated. A good signal difference (GSD) is defined in this range. Subsequently, the detector is set to a gain level of 120 in the following experiments.

4. Results and discussion

The representation of the absorption differences depends essentially on the layer thickness of the applied layer. For this reason, we have determined the maximum penetration depth of polyvinyl chloride (PVC)
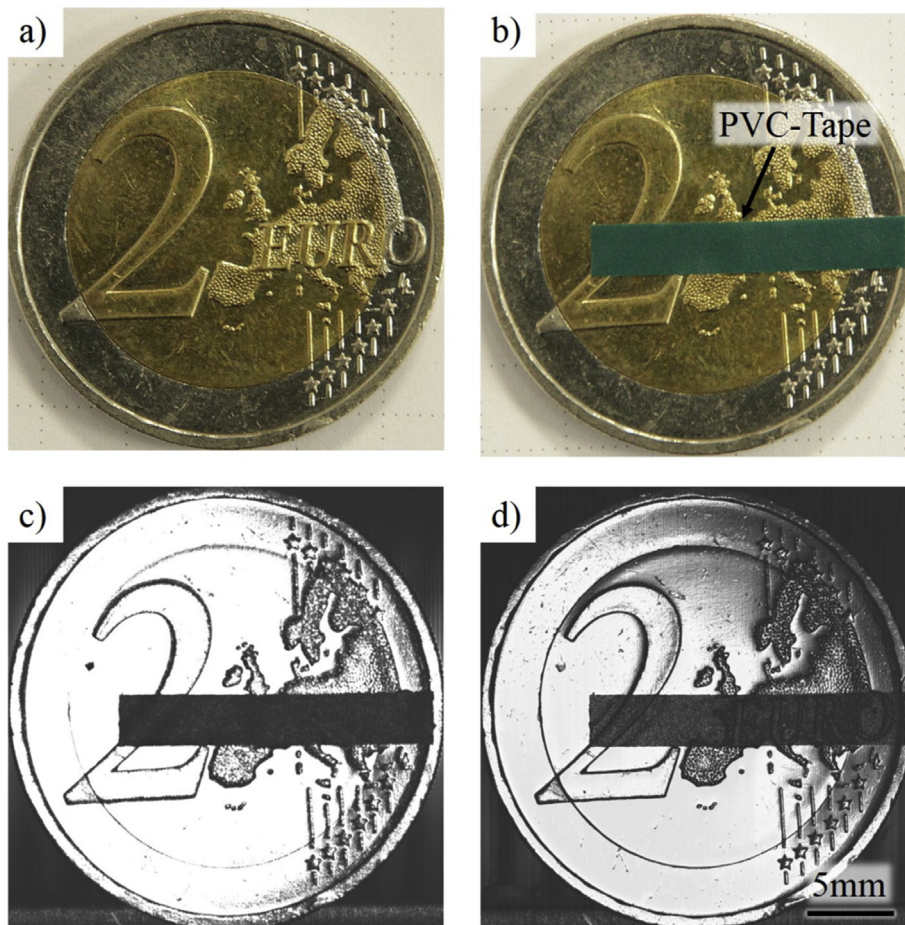

Fig. 7. Presentation of the scan results. a) Image of the non-prepared European coin with a common camera. b) Prepared coin with polymer tape (polyvinyl chloride tape, thickness 130 μm). c) Scan result with prepared sample for the wavelength of 3417 nm d) Scan result with prepared sample for the wavelength of 3584 nm.
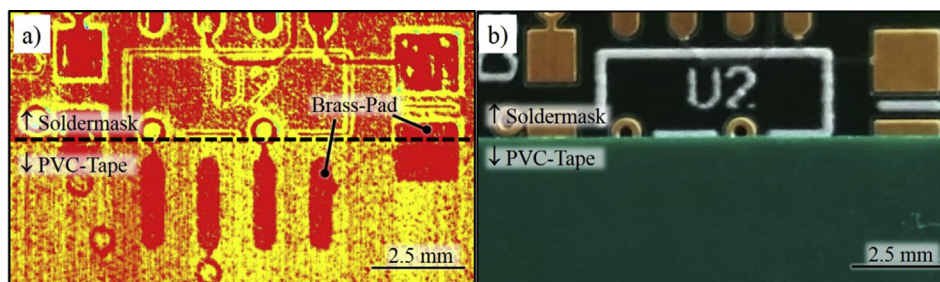
Fig. 9. Preliminary tests for the extraction of solder pads and conductor paths under solder resist and polymer layer (130 μm). a) Absorption differences visualized by the MIR scanner. b) Visual image of the sample with the common camera system.

material using the pre-amplification stage 120 and present the standardized data in Fig. 6. For the determination, we coated a wedge-like structure on a homogeneous gold surface. Using trigonometric correlations of the PVC wedge, we were able to determine the layer thickness. The sample material was scanned at both wavelengths. The resulting image information was compared with the penetration depth calculations.

The analytical investigation of the penetration depth (Fig. 6) indicates a maximum penetration depth for 3417 nm of 20 μm and for 3584 nm of 150 μm. The maximum penetration depth depends on the signal-to-noise ratio (SNR) associated with the measurement. Theoretically, higher penetration depths might be achieved, but the signal cannot be distinguished from noise due to less absorption.

To show the absorption differences in the two lasers using the described optical conditions and knowledge about the maximum penetration depth for PVC, the following scan results are presented in Fig. 7. The scanned object includes flat and irregular surfaces, as well as an area covered by polymer tape (PVC, thickness 130 μm). The European coin contains brass and copper parts. Here, absorption differences in the surface and also in the sample material can be shown. During the scanning process, an area of 25 cm^2 was scanned with a detector with pre-amplification of 120. The scanning time for each wavelength is 50 s with a spatial resolution of 20 μm. Subsequently, the relevant measuring range of the coin was cropped from the total image. The coin depicts the measuring object in its original condition, shown in Fig. 7a. The preparation covers the label of the coin with PVC tape and visualizes the absorption differences for visible light (Fig. 7b).

Absorption differences between 3417 nm (Fig. 7c) and 3584 nm (Fig. 7d) are equivalent on the metallic surfaces of the coin. The absorption differences on flat metallic surfaces between the two wavelengths are insignificant. On uneven surfaces, such as the embossed pattern on the coin, obscure areas are visible. However, these occur predominantly at the edges of the pattern. Due to the refraction of laser light at object edges, the direct reflex is deflected. Due to this, the incident laser light is only partially imaged on the detector. Defined edges of the pattern are imaged comparably for both wavelengths, in contrast to fine uneven structures on the imprint of the map structure of Europe. However, these can only be detected as an average value and appear differently due to the different detection of the direct reflex.

The absorption differences in the measurement results are shown more clearly in Fig. 7c and d by determining the absorbance. For this purpose, the individual measuring points of the absorption images are calculated with each other. The logarithmic representation of the resulting image (Fig. 8) indicates the least differences in absorption.

The homogeneity of absorption is shown by regular colour distribution on the metallic surface of the coin in Fig. 8. Actual differences in absorption between the wavelengths are clearly visible, especially on the PVC tape. The higher the absorption differences between the wavelengths, the more intense the contrasts will be by determining extinction. Differences in absorption enable raying of the applied PVC layer. In

addition, the information on the presence of the PVC layer is preserved. For planar substrates, the absorption difference in the PVC tape can be recovered while the substrate does not have a significant influence.

5. Conclusions

Within the scope of this study, we were able to demonstrate wavelength-selective, fast MIR scanning with data acquisition rates of up to 300 kS/s and a spatial resolution of 20 μm. The special confocal beam path provides a tolerance towards distance variations to the target. By absorption differences in combination with suitable wavelengths, the polymer layer can be distinguished from the background.

In addition, it was possible to illustrate the penetration depth that the described method can achieve. It was evaluated that a fast, flat and confocal absorption measurement in the middle infrared range, from 3.4 μm to 3.6 μm, is possible. The absorption differences are visualized by representing absorbance in pseudo colours. Thus, it is possible to transfer the measuring principle to further applications. Initial experiments showed that the measuring principle could be applied to the control of hidden structures in printed circuit boards (Fig. 9). Conductor tracks can be distinguished despite the superimposed polymer layer and ideally checked for manufacturing defects. In Fig. 9, a printed circuit board was covered partially with a polymer tape (made of PVC).

Due to the differences in absorption, the solder resist around solder pads becomes visible and the PVC can be identified by measurement. Further investigations and applications of this technology can be found in the determination of non-desirable substances on a substrate with long-chain C–H bonds. In particular, substances containing lipids are considered.

By shifting the focus level via the focus unit, slides can be generated for subsequent assembly into a three-dimensional image. Further development work might be required to display three-dimensional absorption differences.

It is therefore conceivable that three-dimensional objects can be examined with the presented measuring system. The focus point can be retraced via the focusing unit. The acquisition of three-dimensional structures or substances on curved substrates, e.g. in quality control, is interesting. However, the shape of the object has to be known before the scan and may have to be captured by a pre-scan.

Declarations

Author contribution statement

Matthias Raedle & Patrick Dörnhofer: Conceived and designed the experiments.

Tim Kümmel: Performed the experiments; Wrote the paper.

Tobias Teumer: Analyzed and interpreted the data.

Björn Wängler & Frank-Jürgen Methner: Contributed reagents, materials, analysis tools or data.

Competing interest statement

The authors declare no conflict of interest.

Additional information

No additional information is available for this paper.

Acknowledgements

References

[1] H.M. Tawancy, M. Hassan, On the degradation mechanism of low-voltage underground cable with poly(vinyl chloride) insulation, J. Mater. Eng. Perform. 25 (2016) 2288–2295.

[2] T. Berer, E. Leiss-Holzinger, A. Hochreiner, J. Bauer-Marschallinger, A. Buchsbaum, Multimodal noncontact photoacoustic and optical coherence tomography imaging using wavelength-division multiplexing, J. Biomed. Opt. 20 (2015), 046013.

[3] H. Keles, F. Susanne, H. Livingstone, S. Hunter, C. Wade, R. Bourdon, A. Rutter, Development of a robust and reusable microreactor employing laser based mid-IR chemical imaging for the automated quantification of reaction kinetics, Org. Process Res. Dev. 21 (2017) 1761–1768.

[4] I.J. Jacobs, J. Li, S.L. Burg, D.J. Bilsky, B.T. Rotondo, M.P. Augustine, P. Stroeve, A.J. Moulé, Reversible optical control of conjugated polymer solubility with sub-micrometer resolution, Am. Chem. Soc. 9 (2015) 1905–1912.

[5] C. Battaglia, X. Yin, M. Zheng, I.D. Sharp, T. Chen, S. McDonnell, A. Azcatl, C. Carraro, B. Ma, R. Maboudian, R.M. Wallace, A. Javey, Hole selective MoOx contact for silicon solar cells, Nano Lett. 14 (2014) 967–971.

[6] A. Katunin, K. Dragan, M. Dziendzikowski, Damage identification in aircraft composite structures: a case study using various non-destructive testing techniques, Compos. Struct. 127 (2015) 1–9.

[7] P.H. Bucksbaum, Ultrafast control, Nature 421 (2003) 593–594.

[8] T. Wang, R. Cao, B. Ning, A.J. Dixon, J.A. Hossack, A.L. Klibanov, Q. Zhou, A. Wang, S. Hu, All-optical photoacoustic microscopy based on plasmonic detection of broadband ultrasound, Appl. Phys. Lett. 107 (2015) 153702.

[9] B. Zhang, L. Lv, T. He, T. Chen, M. Zang, L. Zhong, X. Wang, J. Shen, Y. Hou, Active terahertz device based on optically controlled organometal halide perovskite, Appl. Phys. Lett. 107 (2015), 093301.

[10] W.L. Chan, K. Charan, D. Takhar, K.F. Kelly, R.G. Baraniuk, D.M. Mittelman, A single-pixel terahertz imaging system based on compressed sensing, Appl. Phys. Lett. 93 (2008) 121105.

[11] X. Zhou, P. Zhang, X. Jiang, G. Rao, Influence of maleic anhydride grafted polypropylene on the miscibility of polypropylene/polyamide-6 blends using ATR-FTIR mapping, Vib. Spectrosc. 49 (2009) 17–21.

[12] T. Monouras, M. Vamvakaki, Field responsive materials: photo-, electro-, magnetic- and ultrasound-sensitive polymers, Royal Soc. Chem. 8 (2017) 74–96.

[13] C. Petibois, G. Déléris, Chemical mapping of tumor progression by FT-IR imaging: towards molecular histopathology, Trends Biotechnol. 24 (2006) 455–462.

[14] Q. Li, Y. Tang, Z. Yan, P. Zhang, Identification of trace additives in polymer materials by attenuated total reflection Fourier transform infrared mapping coupled with multivariate curve resolution, Mol. Biomol. Spectroscopy 180 (2017) 154–160.

[15] J.H. Rabe, D.A. Sammour, S. Schulz, B. Munteanu, M. Ott, M. Ochs, P. Hohenberger, A. Marx, M. Platten, C.A. Opitz, D.S. Ory, C. Hopf, Fourier transform infrared microscopy enables guidance of automated mass spectrometry imaging to predefined tissue morphologies, Sci. Rep. 8 (2018) 313.

[16] S. Türker-Kaya, C.W. Huck, A review of mid-infrared and near-infrared imgaing: principles, concepts and applications in plant tissue analysis, Molecules 22 (2017) 1–20.

[17] K. Haase, N. Kröger-Lui, A. Pucci, A. Schönhals, W. Petrich, Real-time mid-infrared imaging of living microorganisms, J. Biophot. 9 (2016) 61–66.

[18] S.G. Kazarian, K.L.A. Chan, ATR-FTIR spectroscopic imaging: recent advances and applications to biological systems, Analyst 138 (2013) 1940–1951.

[19] N. Ramanujam, J. Chen, K. Gossage, R. Richards-Kortum, B. Chance, Fast and noninvasive fluorescence imaging of biological tissues in vivo using a flying-spot scanner, IEEE Trans. Biomed. Eng. 48 (2001) 1034–1041.

[20] P. Ducheyne, K. Healy, D.W. Hutmacher, D.W. Grainger, C.J. Kirkpatrick, Comprehensive Biomaterials II, first ed., Elsevier Ltd., 2017.

[21] W.J. Smith, Modern Optical Engineering, third ed., SPIE Press McGraw-Hill, 2000.

[22] Y. Hu, Theory and Technology of Laser Imaging Based Target Detection, National Defense Industry Press (Springer Nature), 2018.

[23] J. Fraden, Handbook of Modern Sensors, fifth ed., Springer International Publishing Switzerland, 2016.

[24] R.K. Hanson, R.M. Spearrin, C.S. Goldenstein, Spectroscopy and Optical Diagnistics for Gases, Springer International Publishing Switzerland, 2016.

[25] D.F. Swinehart, The Beer-Lambert law, J. Chem. Educ. 39 (1962) 333–335.